ACS APPLIED MATERIALS & INTERFACES

Research Article

www.acsami.org

Transformation of ZnO Nanobelts into Single-Crystalline Mn_3O_4 Nanowires

Chan Woong Na,[†] Seung-Young Park,[†] Jae-Ho Chung,[‡] and Jong-Heun Lee*,[†]

[†]Department of Materials Science and Engineering and [‡]Department of Physics, Korea University, Anam-Dong, Seongbuk-Gu, Seoul 136-713, Republic of Korea

Supporting Information

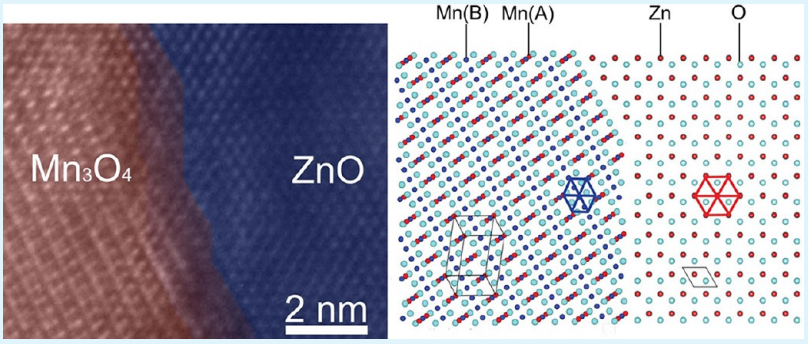

ABSTRACT: Single-crystalline Mn_3O_4 nanowires were prepared using the vapor-phase transformation of ZnO nanobelts. Mn_3O_4-decorated ZnO nanobelts and ZnO–$ZnMn_2O_4$ core–shell nanocables (NCs) were also obtained as reaction intermediates. Heteroepitaxial growth of tetragonal spinel Mn_3O_4 (or $ZnMn_2O_4$) on wurtzite ZnO is a possible reason for the growth of single-crystalline Mn_3O_4 nanowires. Growth interfaces are possibly formed between the wurtzite $(10\bar{1}0)/(2\bar{1}\bar{1}0)$ and spinel $(\bar{1}01)/(\bar{4}11)$ planes. Various one-dimensional homonanostructures and heteronanostructures consisting of *n*-ZnO, *p*-Mn_3O_4, and *p*-$ZnMn_2O_4$ can be used to design high-performance gas sensors.

KEYWORDS: *transformation, gas sensor, heteroepitaxial growth, Mn_3O_4, ZnO*

INTRODUCTION

Manganese oxides including MnO, Mn_3O_4, Mn_2O_3, and MnO_2 have been identified as *p*-type semiconductors because of Mn vacancies within the lattice.[1,2] In particular, Mn_3O_4 is a multifunctional material that has versatile applications such as in combustion catalysts,[3] gas sensors,[4,5] Li-ion batteries,[6] and capacitors.[7] Various methods of synthesizing Mn_3O_4 nanowires (NWs) or nanorods, including the hydrothermal method,[6,8−11] sol−gel process,[12] and thermal evaporation, have previously been developed.[13] Vapor-phase growth is a facile and cost-effective method of growing well-defined single-crystalline NWs with excellent thermal stability at high temperature.[14,15] Although there has previously been a report on the growth of crystalline Mn_3O_4 NWs by thermal evaporation of Mn powders, a high temperature (900 °C) and a long reaction time (2 h) were necessary, and the single crystallinity of the Mn_3O_4 NWs was not demonstrated,[13] indicating that the vapor-phase growth of Mn_3O_4 NWs remains challenging because of the low vapor pressure of Mn sources.

The vapor-phase transformation of template nanoarchitectures can be used as an alternative to synthesize highly crystalline NWs.[16−18] Diverse compositions of NWs can be grown, and various 1-D heteronanostructures such as NWs and nanobelts (NBs) coated with discrete or continuous overlayers can be prepared by tuning the conversion reaction. In particular, the formation of oxide *p*−*n* junctions can enable the production of a variety of useful applications such as light-emitting diodes (LEDs),[19] photoelectrochemical cells (PECs),[20] solar cells,[21] and gas sensors.[22−26]

We have previously used vapor-phase transformation to prepare CoO and Co_3O_4 NWs from a ZnO template.[27] The obtained cobalt oxide NWs exhibited good crystallinity, although they were found to be essentially polycrystalline. The apparent absence of single-crystal formation is ascribed to the low crystallographic matching at the interface between the CoO overlayer and the ZnO underlayer. In this contribution, for the first time, we prepared single-crystalline Mn_3O_4 NWs by the vapor-phase transformation of ZnO nanobelts (NBs). Heteronanostructures such as Mn_3O_4-decorated ZnO NBs and ZnO–$ZnMn_2O_4$ core–shell nanocables (NCs) were also fabricated as reaction intermediates. The main focus was directed at elucidating the mechanism for the transformation from ZnO NBs into single-crystalline Mn_3O_4 NWs, understanding the crystallographic nature of the heteroepitaxial correlation at the ZnO/Mn_3O_4 interface, and designing high-performance gas

Received: August 16, 2012
Accepted: November 13, 2012
Published: November 13, 2012

   dx.doi.org/10.1021/am301670x | *ACS Appl. Mater. Interfaces* 2012, 4, 6565−6572

sensors with various homonanostructures and heteronanostructures consisting of ZnO, $ZnMn_2O_4$, and Mn_3O_4.

EXPERIMENTAL SECTION

ZnO NBs were grown using thermal evaporation on Si wafers and a mixture of ZnO (99.9%, Aldrich), graphite (<20 μm, Aldrich), and Sn (99.8%, Acros) powders. The source (ZnO/graphite/Sn = 1:1:0.01 by weight) was loaded into an Al_2O_3 boat and was positioned in the center of a quartz tube (diameter: 2.5 cm). The Al_2O_3 substrates were placed 5 cm downstream from the source. After the quartz tube was evacuated to $\sim 9 \times 10^{-2}$ Torr, the furnace temperature was increased to 900 °C. The ZnO NBs were formed in a reaction between the source and mixed Ar−O_2 gas (Ar: 100 sccm, O_2: 1 sccm). Mn_3O_4 NWs were prepared using the following procedure: The as-grown ZnO NBs on Si wafers and $MnCl_2$ (99.99%, Aldrich) were placed in the downstream and upstream parts of the Al_2O_3 boat (4 cm long), respectively. After the quartz tube was evacuated to $\sim 9 \times 10^{-2}$ Torr, the furnace temperature was increased to 500−750 °C and maintained at the reaction temperature for 20 min. During the reaction, a mixture of Ar and O_2 (Ar: 200 sccm, O_2: 10 sccm) was provided as the reaction gas. The Mn_3O_4-decorated ZnO NBs were prepared at 500 °C, and ZnO−$ZnMn_2O_4$ core−shell NCs were obtained at 600 °C. When the reaction temperature was elevated to 750 °C, ZnO NBs were transformed into phase-pure Mn_3O_4 NWs.

The structural properties of the NWs were investigated using X-ray diffraction (XRD, Rigaku D/MAX-2500 V/PC), scanning electron microscopy (SEM, Hitachi S-4700), field-emission transmission electron microscopy (FE TEM, FEI TECNAI G2 200 kV, and JEOL JEM 3010), and energy-dispersive X-ray spectroscopy (EDS). Raman spectroscopy (Princeton instrument, Acton SP 2500) was performed using the 514.5 nm line of an argon-ion laser. The chemical states of the films were determined using X-ray photoelectron spectroscopy (ULVAC-PHI, PHI 5000 VersaProbeTM) with an Al Kα radiation (1486.6 eV) source. The binding energies were corrected for specimen charging by referencing the C 1s peak at 284.6 eV.

RESULTS AND DISCUSSION

SEM and TEM. Clean-surfaced single-crystalline ZnO NBs were prepared using thermal evaporation (Figure S1a-b, Supporting Information). The width of the ZnO NBs ranged from 50 to 80 nm (Figure S1b, Supporting Information). The selected-area electron diffraction (SAED) pattern (inset in Figure S1c, Supporting Information) suggests that the ZnO NBs with (0001) and $(2\bar{1}\bar{1}0)$ surfaces grow along the $[01\bar{1}0]$ direction. From the high-resolution TEM image of the surface of the ZnO NBs, the $(01\bar{1}0)$ fringes are separated by a distance of about 2.81 Å (Figure S1d, Supporting Information).

Semielliptical Mn_3O_4 nanoparticles were uniformly deposited onto the surface of the ZnO NBs by thermal evaporation of $MnCl_2$ powders at 500 °C in 4.76% O_2 (Figures 1a and b). The diameters of Mn_3O_4-decorated ZnO NBs ranged from 50 to 80 nm. The semielliptical Mn_3O_4 nanoparticles had lateral lengths in the range of 2−10 nm (Figure 1c). The lattice-resolved TEM image (Figure 1d) of the Mn_3O_4-decorated ZnO NBs shows that the $(10\bar{1}0)$ fringes of ZnO and the $(\bar{1}01)$ fringes of the Mn_3O_4 particles are separated by 2.81 and 4.92 Å, respectively, and are nearly parallel to each other. The compositions of the Mn_3O_4 nanoparticles were identified from the line-scan profiles of Zn, Mn, and O by using energy-dispersive X-ray spectroscopy (EDS) (Figure S2, Supporting Information).

Detailed inspection of the lattice-resolved TEM images revealed that the Mn_3O_4 nanoparticles not only grew on the ZnO NBs along a particular direction but also formed the atomic interfaces necessary for heteroepitaxial growth. Figure 2a shows a close-up picture of an interface between two phases. On the right side of the red dashed line is the wurtzite ZnO lattice, in which

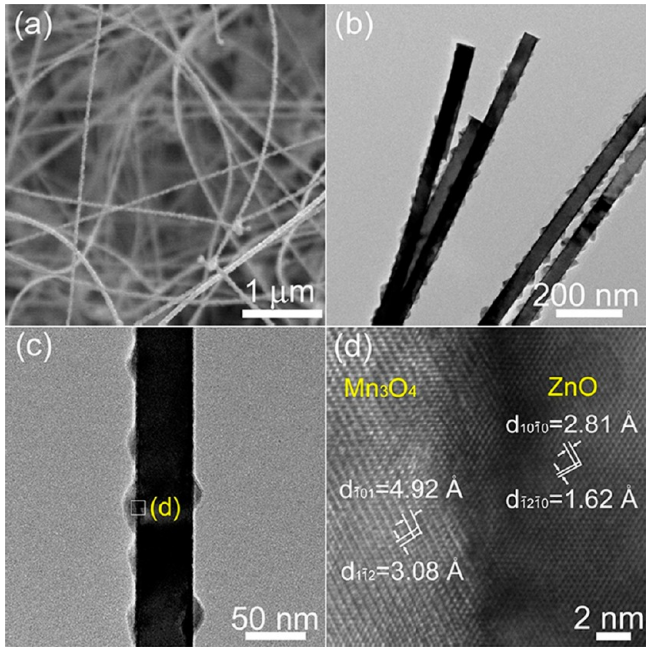

Figure 1. Morphologies and crystal structures of Mn_3O_4-decorated ZnO NBs: (a) SEM image of Mn_3O_4-decorated ZnO NBs grown on Si substrates, (b) and (c) TEM images of Mn_3O_4-decorated ZnO NBs, and (d) lattice-resolved TEM image of Mn_3O_4-decorated ZnO NBs.

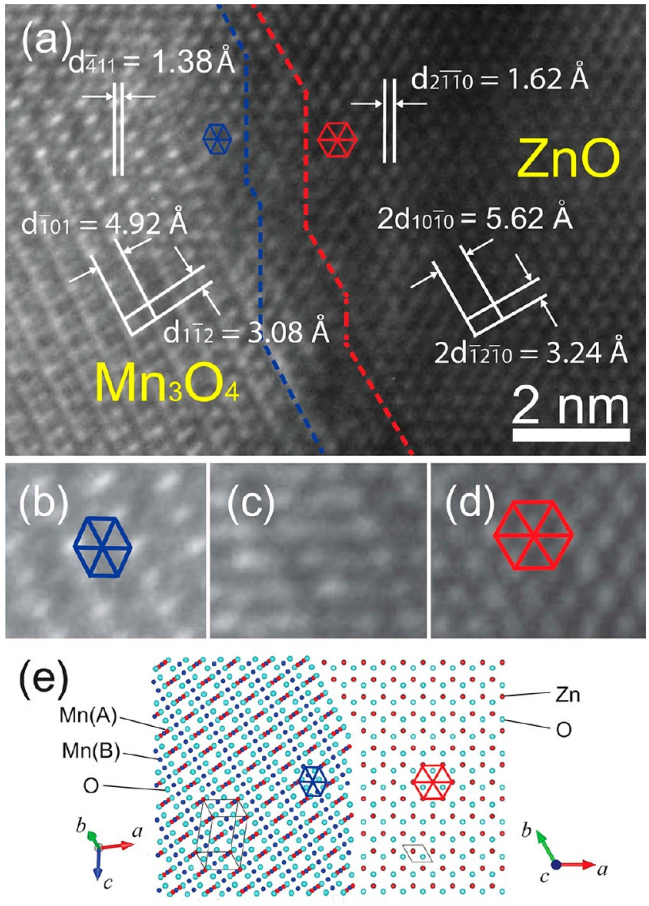

Figure 2. (a) Section of lattice-resolved TEM image revealing the interface between Mn_3O_4 and ZnO. Blue and red dashed lines are proposed atomic interfaces, as discussed in the text. Close-up views of (b) Mn_3O_4 lattice, (c) region containing mixed lattice structures, and (d) ZnO lattice. (e) Proposed model of atomic interface between spinel and wurtzite lattices.

dx.doi.org/10.1021/am301670x | ACS Appl. Mater. Interfaces 2012, 4, 6565−6572

the 6-fold symmetry of Zn sites is clearly visible (Figure 2d). Note that the straight segments of the wurtzite ZnO lattice are parallel to $(2\bar{1}\bar{1}0)$ and $(10\bar{1}0)$ fringes. On the left side of the blue dashed line is the spinel Mn_3O_4 lattice, in which the 6-fold symmetry is reduced to 2-fold, and each atomic image is elongated along $[\bar{1}01]$ directions (Figure 2b). The elongated atomic image is ascribed to one A and two B sites of the spinel AB_2O_4 lattice, partially overlapping when viewed in the [131] zone of the lattice (Figure 2e). The straight segments in this case are parallel to the $(\bar{1}01)$ and $(\bar{4}11)$ fringes. A region exhibiting mixed properties is shown between the two dashed lines, and the mixed properties suggest that the interfaces consist of several atomic layers (Figure 2c). Such mixed properties are ascribed to the accommodation of the mismatch between the two lattices. Figure 2e shows the atomic lattice model with the spinel lattice projected on its [131] zone and the wurtzite projected on its [0001] zone, which is reasonably consistent with the lattices observed in the TEM image except in the region exhibiting mixed lattice properties. It is apparent that the 6-fold pseudosymmetry is maintained along the interface between the two lattices.

As the reaction temperature was increased to 600 °C, the ZnO NBs became completely coated with continuous $ZnMn_2O_4$ overlayers, which led to the formation of ZnO−$ZnMn_2O_4$ core−shell NCs (Figure 3a). The shell layer was 17−35 nm

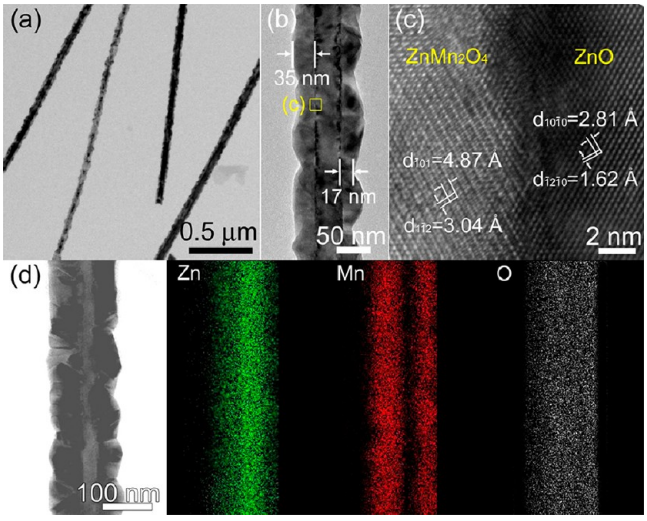

Figure 3. Morphologies and crystal structures of ZnO−$ZnMn_2O_4$ NCs: (a) and (b) TEM images of ZnO−$ZnMn_2O_4$ NCs grown on Si substrates. (c) Lattice-resolved image of ZnO−$ZnMn_2O_4$ NCs. (d) EDS elemental mapping of Zn, Mn, and O.

thick (Figure 3b). We found that the angular relations between the lattice fringes observed in ZnO and those observed in $ZnMn_2O_4$ were essentially unchanged, even after coating had been completed (Figure 3c), because the spinel lattice is virtually identical in Mn_3O_4 and in $ZnMn_2O_4$ and because conversion between the two involves only a small change, for example, reducing the $(\bar{1}01)$ lattice spacing from 4.92 to 4.87 Å. The formation of ZnO−$ZnMn_2O_4$ core−shell NCs is also supported by the results of the EDS elemental mappings of Zn, Mn, and O (Figure 3d). When the reaction temperature was further elevated to 750 °C, the ZnO−$ZnMn_2O_4$ core−shell NCs were completely converted into Mn_3O_4 NWs (Figure 4a). A TEM image of a NW and the corresponding SAED pattern (at the [131] zone axis) reveal a single-crystalline Hausmannite Mn_3O_4 NW (Figure 4b).

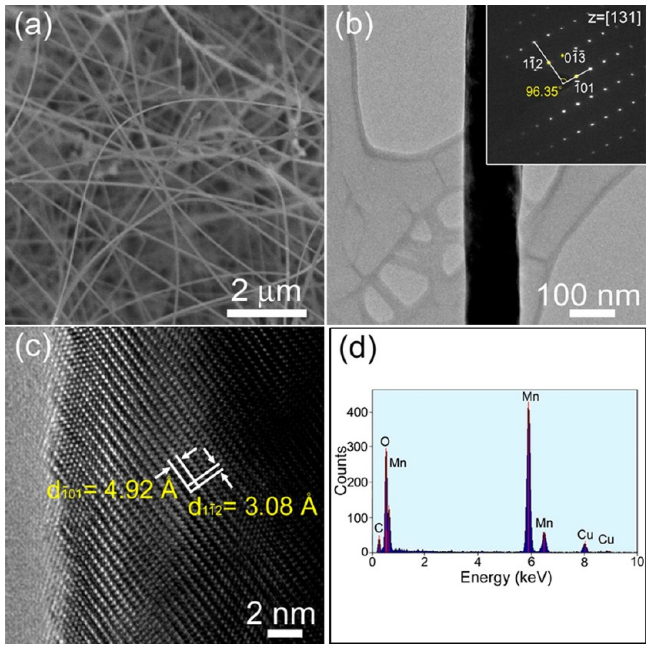

Figure 4. Morphologies and crystal structures of Mn_3O_4 NWs: (a) SEM image of Mn_3O_4 NWs grown on Si substrates, (b) and (c) TEM images of Mn_3O_4 NWs (inset SAED pattern for Mn_3O_4 NWs), and (d) EDS spectrum for Mn_3O_4 NWs.

In the lattice-resolved TEM image (Figure 4c) of the Mn_3O_4 NW, the $(\bar{1}01)$ fringes and the $(1\bar{1}2)$ fringes are separated by 4.92 and 3.08 Å, respectively. The results of the EDS analysis indicate that the ZnO was completely converted into Mn_3O_4 (Figure 4d). The SAED patterns were generated for four different spots on a Mn_3O_4 NW (Figure 5, yellow area) and were

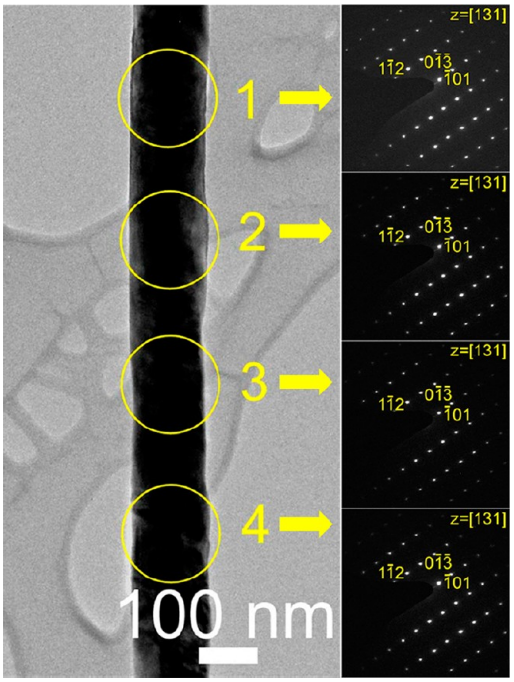

Figure 5. TEM image and SAED patterns for the Mn_3O_4 NW.

analyzed along the longitudinal direction to double-check the single crystallinity of the Mn_3O_4 NWs. The SAED patterns

dx.doi.org/10.1021/am301670x | ACS Appl. Mater. Interfaces 2012, 4, 6565−6572

indicated the presence of a very large area of crystal domains (at least >1 μm), and the TEM analysis did not show any grain boundaries within the NWs.

When all the lattice-resolved TEM images and SAED data were compared, we found that the crystallographic orientations of $ZnMn_2O_4$ and Mn_3O_4 are always maintained with respect to the growth direction of the ZnO NBs. The long edges of the ZnO NBs are parallel with the $[01\bar{1}0]$ direction, which has previously been well documented[28] and with which the results in the current work are consistent. Therefore, the $[10\bar{1}0]$ direction is rotated by 60° with respect to the long edges. The $[\bar{1}01]$ directions of the tetragonal spinels are always found within a few degrees (<3°) of the $[10\bar{1}0]$ direction of ZnO in both partially converted (Figures 1d and 3c) and fully converted (Figures 4c and 5). These observations strongly suggest that the tetragonal spinels exhibit a strong tendency toward heteroepitaxial growth on the ZnO NBs. We suppose that the symmetry of the tetragonal structure because of Jahn–Teller active Mn^{3+} ions played an important role in forming atomic interfaces with sufficiently low lattice mismatch. This behavior is in contrast to ZnO–Co_3O_4 NBs in which shell layers grow with good crystallinity but lack directionality.[27]

X-ray Diffraction Patterns (XRD). Figure S3 (Supporting Information) shows the XRD patterns for the ZnO NBs, Mn_3O_4-decorated ZnO NBs, ZnO–$ZnMn_2O_4$ core–shell NCs, and Mn_3O_4 NWs. The XRD pattern for the ZnO NBs confirms the highly crystalline wurtzite structure (JCPDS No. 36-1451) (Figure S3a, Supporting Information). Small peaks associated with Mn_3O_4 were observed in the XRD pattern for the Mn_3O_4-decorated ZnO NBs (Figure S3b, Supporting Information). The intensities of the peaks associated with either Mn_3O_4 or $ZnMn_2O_4$ increase in the XRD pattern for the core–shell NCs (Figure S3c, Supporting Information). The positions of the peaks associated with Mn_3O_4 (JCPDS No. 24-0734, a = 5.762 Å, c = 9.469 Å) are similar to those of the peaks associated with $ZnMn_2O_4$ (JCPDS No. 24-1133, a = 5.720 Å, c = 9.245 Å). We measured the Raman scattering of the ZnO NBs, ZnO–$ZnMn_2O_4$ core–shell NCs, and Mn_3O_4 NWs (Figure 6) to distinguish between the Mn_3O_4 and $ZnMn_2O_4$.

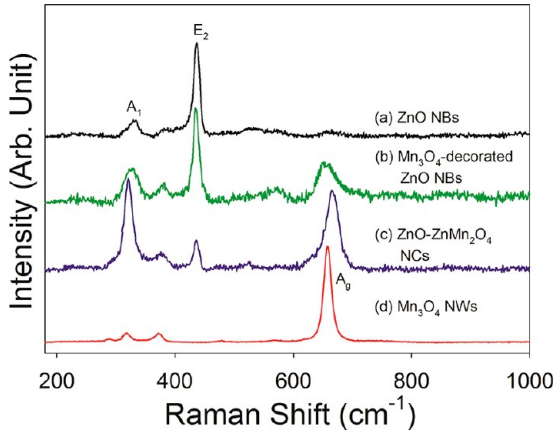

Figure 6. Raman spectra for (a) pristine ZnO NBs, (b) Mn_3O_4-decorated ZnO NBs, (c) ZnO–$ZnMn_2O_4$ core–shell NCs, and (d) Mn_3O_4 NWs.

Raman Spectroscopy. The Raman spectrum for the ZnO NBs exhibits two Raman active peaks at 334.8 (A_1) and 442.1 cm^{-1} (E_2) (Figure 6a). The Raman spectrum for Mn_3O_4 exhibits three Raman active peaks at 318.5, 371.8, and 657.5 cm^{-1} (Figure 6d). The $ZnMn_2O_4$ has a tetragonal crystal structure in which the Zn^{2+} ions occupy the tetrahedral sites and the Mn^{3+} ions occupy the octahedral sites. In the Raman spectrum for the Mn_3O_4 structure, the Raman peak at 657.5 cm^{-1} (A_g) is attributed to characteristics of the octahedral sites, and the peaks at 318.5 and 371.8 cm^{-1} are likely related to the combined vibrations of tetrahedral sites and the motions of oxygen atoms in octahedral sites in $Zn_yMn_{3-y}O_4$.[29] The position of the A_g peak in the Raman spectrum for the Mn_3O_4 NWs (657.5 cm^{-1}, Figure 6d) is similar to that of the A_g peak in the Raman spectrum for the Mn_3O_4-decorated ZnO NBs (655 cm^{-1}, Figure 6b), but it occurs at a significantly lower wavenumber than that of the A_g peak in the Raman spectrum for the ZnO–$ZnMn_2O_4$ core–shell NCs (Figure 6c). This result indicates that the decorated nanoparticles and continuous shell layers consist of the Mn_3O_4 and $ZnMn_2O_4$ phases, respectively. Accordingly, the peaks in the XRD spectrum for the core–shell configured NCs can be attributed to the $ZnMn_2O_4$ phase rather than to the Mn_3O_4 phase.

X-ray Photoelectron Spectroscopy (XPS). The survey-scanned and fine-scanned XPS spectra are shown in Figure 7, and the results are summarized in Table S1 (Supporting Information). The Zn $2p_{3/2}$ peak in the spectrum for the pure ZnO NBs is located at 1021.8 eV and is symmetric (Figure 7b). In contrast, the same peaks in the spectra for the Mn_3O_4-decorated ZnO NBs and the ZnO–$ZnMn_2O_4$ core–shell NCs are asymmetric, and the peaks could be deconvoluted into Zn–O and Zn–Mn bands. The binding energy associated with the Zn–O band remained the same (1021.8 eV) regardless of the Mn-containing layer. In comparison, the binding energies associated with the Zn–Mn band for the Mn_3O_4-decorated ZnO NBs and the ZnO–$ZnMn_2O_4$ core–shell NCs were 1020.7 and 1022.7 eV, respectively. The Mn $2p_{3/2}$ peaks in the spectra for the Mn_3O_4-decorated ZnO NBs, ZnO–$ZnMn_2O_4$ core–shell NCs, and Mn_3O_4 NWs could be deconvoluted into Mn(II)–O and Mn(III)–O bands. The area % values of the Mn(III)–O bands in the spectra for the Mn_3O_4-decorated ZnO NBs and Mn_3O_4 NWs are similar (68 and 67%), which is consistent with the composition of Mn_3O_4. The area % of the Mn(III)–O band in the spectrum for the ZnO–$ZnMn_2O_4$ core–shell NCs is significantly higher (90%), indicating again that the Mn component in the core–shell NCs can be identified as $ZnMn_2O_4$ rather than Mn_3O_4.

Transformation Mechanism. Considering the phases and configurations of the various reaction products and on the basis of the relevant data in the literature for the cation exchange reaction,[30] we propose the following transformation reactions and mechanism. The partial transformation from the surface region of ZnO to the $ZnMn_2O_4$ shell layer can be attributed to the relatively high vapor pressure of $MnCl_2$ and to the efficient cation exchange reaction that occurs at high temperature (600 °C), which can be explained by the following reaction

$$3ZnO(s) + 2MnCl_2(g) + \frac{1}{2}O_2(g) \rightarrow ZnMn_2O_4(s) + 2ZnCl_2(g) \quad (1)$$

This reaction is feasible considering that the reaction temperature (600 °C) is close to the melting point of $MnCl_2$(s) (652 °C). The $ZnMn_2O_4$ can be further converted into the pure Mn_3O_4 phase under the very high vapor pressure of $MnCl_2$ and by the enhanced cation exchange reaction at 750 °C from the following reaction

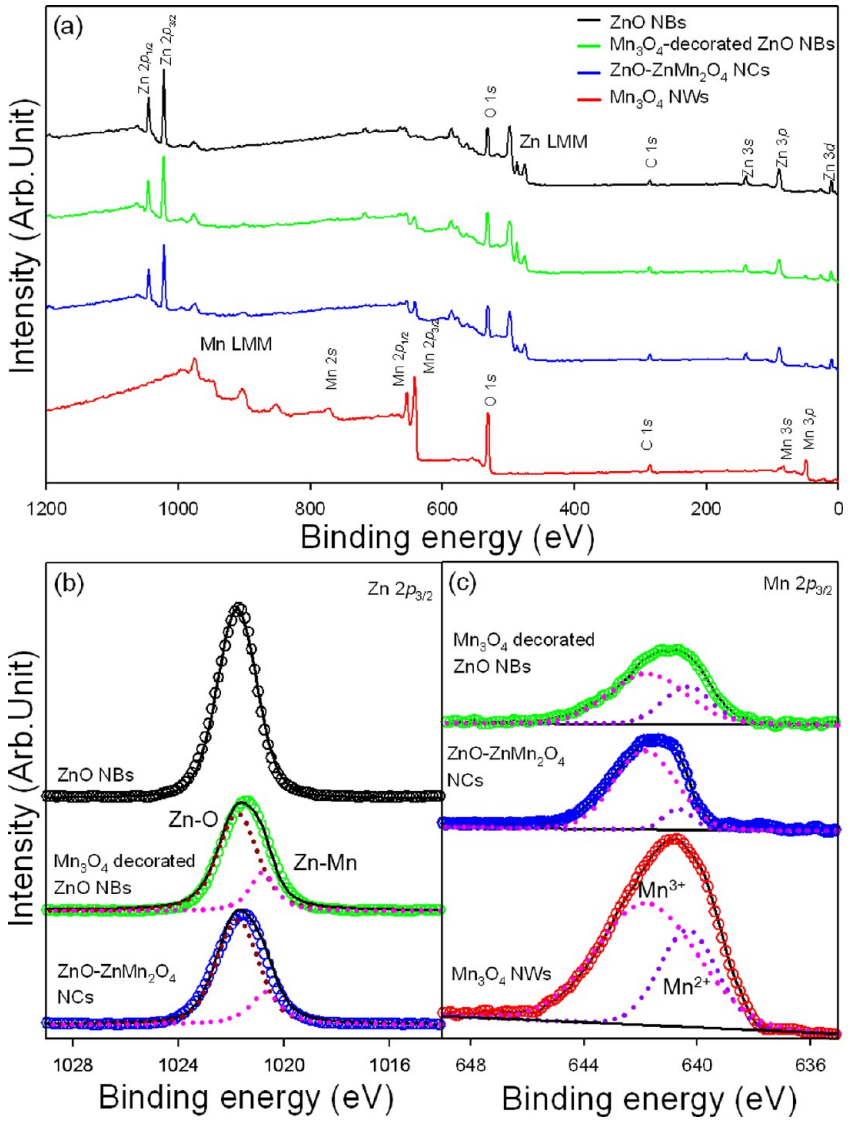

Figure 7. XPS results: (a) full-range, (b) Zn $2p_{3/2}$, and (c) Mn $2p_{3/2}$ spectra.

$$ZnMn_2O_4(s) + MnCl_2(g) \rightarrow Mn_3O_4(s) + ZnCl_2(g) \quad (2)$$

The reaction for the direct transformation of ZnO to Mn_3O_4 can be given by combining the previous two reactions as follows

$$3ZnO(s) + 3MnCl_2(g) + \frac{1}{2}O_2(g) \rightarrow Mn_3O_4(s) + 3ZnCl_2(g) \quad (3)$$

The overall chemical reaction for the transformation indicates that the vapor pressure of $MnCl_2$ and the cation exchange reaction between Zn and Mn should be carefully controlled by tuning the reaction temperature. For instance, the decoration of the Mn_3O_4 nanoparticles on the ZnO NBs without the formation of the $ZnMn_2O_4$ phase at 500 °C can be ascribed to an insufficient cation exchange reaction between Zn and Mn because of the relatively low vapor pressure of $MnCl_2(g)$ and the low reaction temperature. It is also important that sufficient oxygen should be provided during the reaction.

Gas Sensing Characteristics. The sensing transients to 100 ppm C_2H_5OH at 400 °C are plotted in Figure 8. The pure ZnO- or Mn_3O_4-decorated ZnO NBs exhibited *n*-type gas sensing behaviors; that is, the resistance of the sensors decreased in response to reducing gas (Figures 8a and b). This result indicates that the conduction in the Mn_3O_4-decorated ZnO NBs occurs along the *n*-type ZnO NB core rather than the discrete configuration of *p*-type Mn_3O_4 nanoparticles. The R_a/R_g values ($S = R_a/R_g$, R_a: resistance in air, R_g: resistance in gas) were used to measure the responses of the sensors produced with either the pure ZnO or Mn_3O_4-decorated ZnO NBs to various gases. In contrast, the gas sensors produced with either the ZnO–$ZnMn_2O_4$ core–shell NCs or Mn_3O_4 NWs exhibited *p*-type gas sensing behaviors; that is, the resistance of the sensors increased upon exposure to reducing gases (Figures 8c and d). Note that both $ZnMn_2O_4$ and Mn_3O_4 are *p*-type semiconductors.[1,31] This result indicates that the conduction and chemoresistive variation in ZnO–$ZnMn_2O_4$ core–shell NCs are dominated by continuous *p*-type 17–35-nm-thick $ZnMn_2O_4$ shell layers. Accordingly, the R_g/R_a values were used to measure the responses of the sensors produced with either ZnO–$ZnMn_2O_4$ core–shell NCs or Mn_3O_4 NWs to various gases.

The gas responses of pure ZnO NBs, Mn_3O_4-decorated ZnO NBs, ZnO–$ZnMn_2O_4$ NCs, and Mn_3O_4 NWs to various reducing gases (100 ppm C_2H_5OH, NH_3, CO, C_3H_8, and H_2)

dx.doi.org/10.1021/am301670x | ACS Appl. Mater. Interfaces 2012, 4, 6565–6572

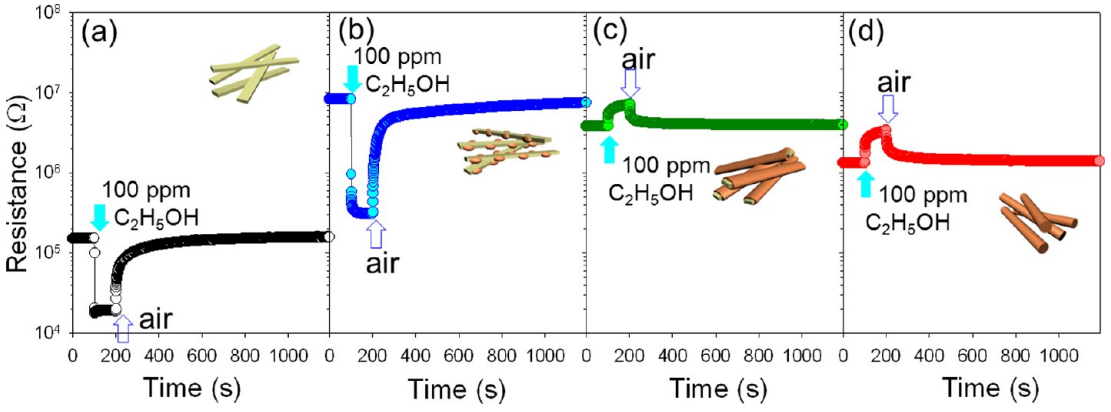

Figure 8. Sensing transients to 100 ppm C_2H_5OH at 400 °C: (a) ZnO NBs, (b) Mn_3O_4-decorated ZnO NBs, (c) ZnO−$ZnMn_2O_4$ NCs, and (d) Mn_3O_4 NWs.

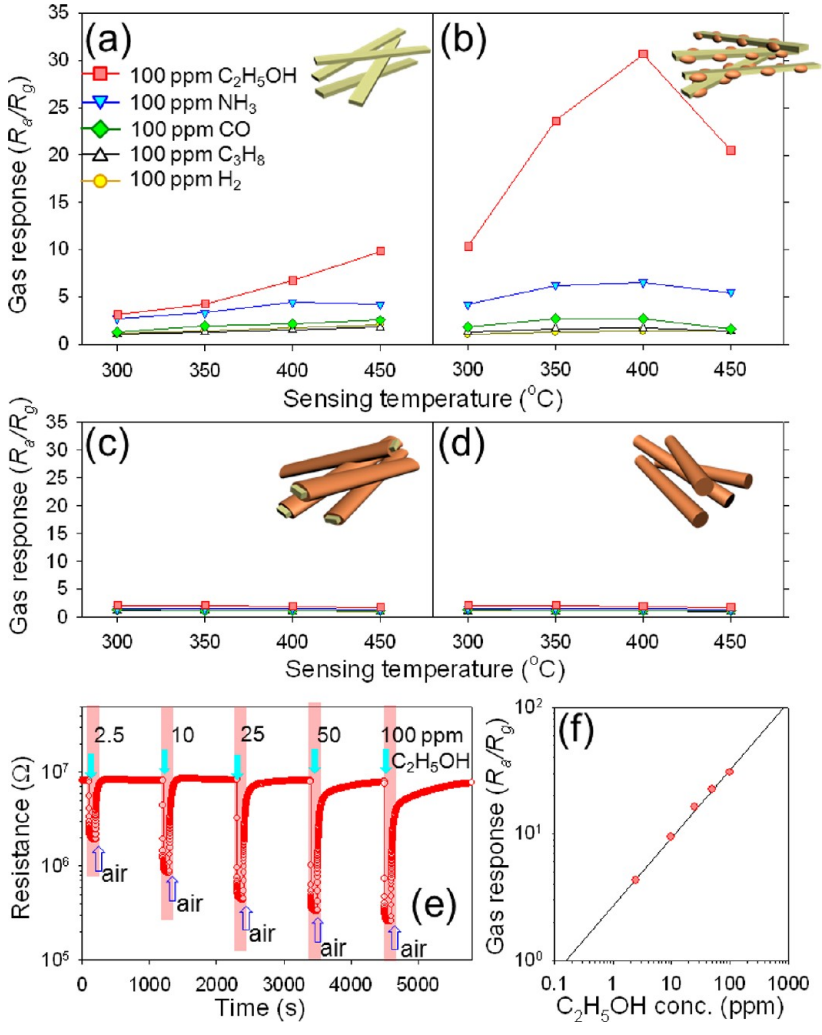

Figure 9. Gas responses (R_a/R_g or R_g/R_a; R_a: resistance in air and R_g: resistance in gas) to 100 ppm C_2H_5OH, NH_3, CO, C_3H_8, and H_2 gases measured in the range 300−450 °C for sensors produced with: (a) ZnO NBs, (b) Mn_3O_4-decorated ZnO NBs, (c) ZnO−$ZnMn_2O_4$ NCs, and (d) Mn_3O_4 NWs. (e) Dynamic transient for sensitivity of the gas sensor produced with the Mn_3O_4-decorated ZnO NBs to various concentrations of C_2H_5OH and (f) responses of Mn_3O_4-decorated ZnO NBs to various concentrations of C_2H_5OH measured at 400 °C plotted as a function of C_2H_5OH concentration.

were measured in the range of 300−450 °C (Figures 9a−d). The responses of all four sensors to 100 ppm C_2H_5OH were higher than the responses of all four sensors to 100 ppm NH_3, CO, C_3H_8, and H_2. However, the absolute and relative responses to C_2H_5OH were significantly different for each sensor, depending on the sensor materials or the configurations of the *p*-type overlayers. Although the pure ZnO NBs exhibited selective detection of C_2H_5OH at 400 and 450 °C (Figure 9a), the highest response and selectivity to C_2H_5OH were achieved for the sensor produced with the Mn_3O_4-decorated ZnO NBs (Figure 9b). Note that the C_2H_5OH responses of Mn_3O_4-decorated ZnO NBs are significantly higher than those to the other gases over the

dx.doi.org/10.1021/am301670x | ACS Appl. Mater. Interfaces 2012, 4, 6565−6572

entire sensor temperature range (300−450 °C). The ratios of the sensor responses to C_2H_5OH and to the other gases ($S_{ethanol}/S_{gas} = (R_a/R_g)_{ethanol}/(R_a/R_g)_{gas}$) were calculated to quantify the selectivity of the responses of the sensors to C_2H_5OH. The $S_{ethanol}/S_{gas}$ values for NH_3, CO, C_3H_8, and H_2 of Mn_3O_4-decorated ZnO NBs at 400 °C were 4.69, 11.31, 18.14, and 21.14, respectively, which were markedly higher than those of pure ZnO NBs (1.75, 3.53, 5.15, and 4.60, respectively). This result can be attributed to the catalytic promotion of the gas sensing reaction by the discrete configuration of the Mn_3O_4 nanoparticles and is consistent with our previous results[24,25,32] on enhancing gas selectivity by decorating ZnO NBs with various *p*-type nanoparticles. In contrast, the gas responses of ZnO−$ZnMn_2O_4$ NCs or the Mn_3O_4 NWs to the various gases were similar (1.03−2.14), and no significant selectivity to a specific gas was observed for those sensors (Figures 9c and d). This result indicates that decorating discrete Mn_3O_4 nanoparticles on ZnO NBs is a very effective method of designing a highly selective and sensitive C_2H_5OH sensor.

The dynamic transients of the Mn_3O_4-decorated ZnO NBs to various concentrations of C_2H_5OH in the range 2.5−100 ppm at 400 °C reveal that the sensor exhibits stable sensing and recovery characteristics (Figure 9e). From the linear regression line fit of the responses of the sensor plotted as a function of C_2H_5OH concentration, the lower limit for the detection of C_2H_5OH was estimated as 0.15 ppm when $R_a/R_g > 1.2$ was used as the standard for gas detection (Figure 9f), which is significantly lower than the limit used for screening an intoxicated driver ($[C_2H_5OH] >$ 200 ppm).[33] The variation in the response and selectivity of the sensor to various gases significantly depends on the materials and heteronanostructures used in the sensor, and this should be understood in the framework of the gas sensing mechanism. The gas responses of *n*-type ZnO NBs or Mn_3O_4-decorated ZnO NBs to various gases are higher than those of *p*-type ZnO−$ZnMn_2O_4$ core−shell NCs or Mn_3O_4 NWs (Figures 8a−d). Although the gas response depends on the sensing materials, the conduction mechanisms of *n*- and *p*-type oxide semiconductors can also induce different chemoresistive variations. In *n*-type oxide NBs or NWs, the adsorption of negatively charged oxygen forms an electron depletion layer near the surface.[34] The ZnO NBs (50−80 nm) used in the present study are more than two times wider than the typical thickness of the electron depletion layer in ZnO (5−10 nm).[35] Under this condition, each NW consists of a resistive electron depletion layer at the outer part and the semiconducting layer at the inner part, and the chemoresistive variation at the inter-NW contacts rather than that at the intra-NWs plays a more significant role in gas sensing.[36] In contrast, the adsorption of negatively charged oxygen on *p*-type-oxide NBs or NWs forms a hole accumulation layer near the surface. When the thicknesses (or diameters) of the NBs (or the NWs) are thicker than twice the thickness of the hole-accumulation layer, the conduction across the NB or NW network can be explained by parallel competition between those along the hole-accumulation surface layer and the resistive inner layer. Note that the inter-NB or inter-NW contacts in *p*-type oxides no longer play significant roles in the gas sensing reaction and that the decrease in the thickness of the hole-accumulation layer upon exposure to the reducing gas is responsible for the increase in resistance. In this conduction model, adjusting the thickness of the hole-accumulation layer usually does not lead to very high gas response unless the hole-accumulation layer becomes extremely thin.[37] The low gas responses in *p*-type ZnO−$ZnMn_2O_4$ core−shell NCs or the Mn_3O_4 NWs can be partly understood from this perspective. Nevertheless, the importance and potential of *p*-type oxide semiconductors should not be underestimated because the gas responses of *p*-type oxide semiconductors to various gases can be enhanced by noble-metal doping and metal oxide additives to promote the catalytic reaction and changes in the hole-accumulation layer.[38] Moreover, considering that most *p*-type oxide semiconductors such as Mn_3O_4, CuO, Cr_2O_3, and Co_3O_4 are well-known catalytic materials that promote chemical reactions,[3,39−41] the preparation of various compositions and configurations of one-dimensional *p*-type nanostructures such as ZnO−$ZnMn_2O_4$ core−shell NCs and Mn_3O_4 NWs in the present study may be used to detect a specific gas in a selective manner. The R_a values of four different sensors were compared to understand the conduction behaviors and gas sensing reactions of 1-dimensional nanostructures. The R_a values of the Mn_3O_4-decorated ZnO NBs are significantly higher than those of the pure ZnO NBs (Figure S4, Supporting Information). When *p*-type Mn_3O_4 is decorated onto ZnO NBs in a discrete configuration, the electron depletion layer underneath the Mn_3O_4 nanoparticles will be extended to a radial direction of ZnO NBs, which decreases the cross-sectional area for conduction along the semiconducting inner region (*n*-type). This explains the 36.5- to 82.4-fold increase in R_a by decorating Mn_3O_4 nanoparticles onto the ZnO NBs. Accordingly, the electron injection and consequent thinning of the electron-depletion layer upon exposure to the reducing gas leads to higher chemoresistive variation in Mn_3O_4-decorated ZnO NBs than in pure ZnO NBs. The higher R_a values for ZnO−$ZnMn_2O_4$ NCs can be explained by the high resistivity of $ZnMn_2O_4$, the thin configuration of the shell layer, and/or the extension of the hole-depletion layer at the interface between the *p*-type $ZnMn_2O_4$ and the *n*-type ZnO layers.

These results clearly demonstrate that not only gas response but also selectivity can be enhanced or tuned by the configurational design of radial *p*−*n* junctions in 1-dimensional heteronanostructures. Although the ZnO−$ZnMn_2O_4$ NCs and Mn_3O_4 NWs did not exhibit promising gas sensing characteristics, those nanostructures can still be used in various applications. For example, the ZnO−$ZnMn_2O_4$ NCs produced in the present study can be applied to highly efficient all-oxide LEDs,[19] and oxide heteronanostructures can be valuable material platforms for designing PECs[20] and solar cells.[21]

CONCLUSIONS

Various 1-D homonanostructures and heteronanostructures containing ZnO, Mn_3O_4, or $ZnMn_2O_4$ (such as Mn_3O_4 NWs, Mn_3O_4-decorated ZnO NBs, and ZnO−$ZnMn_2O_4$ NCs) were synthesized using vapor-phase transformation of ZnO NBs. The heteroepitaxial correlation at the interface between ZnO and Mn_3O_4 or that at the interface between ZnO and $ZnMn_2O_4$ provided a novel mechanism for growing single-crystalline Mn_3O_4 NWs. Various 1-D oxide *n*-type and *p*-type nanostructures and *p*−*n* junction semiconductors can provide versatile and powerful platforms for designing high-performance gas sensors, LEDs, and other functional devices.

ASSOCIATED CONTENT

Supporting Information

XPS table, X-ray diffraction patterns, sensor resistance in air, EDS results, and SEM and TEM images of hetero-NWs/NBs and homo-NWs/NBs. This material is available free of charge via the Internet at http://pubs.acs.org.

AUTHOR INFORMATION

Corresponding Author

*E-mail: jongheun@korea.ac.kr.

Notes

The authors declare no competing financial interest.

ACKNOWLEDGMENTS

This work was supported by a grant (No.R0A-2008-000-20032-0) from the National Research Foundation (NRF) of Korea funded by the Korean government Ministry of Education, Science, and Technology (MEST).

REFERENCES

(1) Dorris, S. E.; Mason, T. O. *J. Am. Ceram. Soc.* **1988**, *71*, 379−385.
(2) Kwon, K. D.; Refson, K.; Sposito, G. *Phys. Rev. Lett.* **2008**, *100*, 146601.
(3) Baldi, M.; Finocchio, E.; Milella, F.; Busca, G. *Appl. Catal., B* **1998**, *16*, 43−51.
(4) Xu, C.-N.; Miyazaki, K.; Watanabe, T. *Sens. Actuators B* **1998**, *46*, 87−96.
(5) Zhang, L.; Zhou, Q.; Liu, Z.; Hou, X.; Li, Y.; Lv, Y. *Chem. Mater.* **2009**, *21*, 5066−5071.
(6) Li, P.; Nan, C. Y.; Wei, Z.; Lu, J.; Peng, Q.; Li, Y. D. *Chem. Mater.* **2010**, *22*, 4232−4236.
(7) Fang, M.; Tan, X.; Liu, M.; Kang, S.; Hu, X.; Zhang, L. *CrystEngComm* **2011**, *13*, 4915−4920.
(8) Du, J.; Gao, Y.; Chai, L.; Zou, G.; Li, Y.; Qian, Y. *Nanotechnology* **2006**, *17*, 4923−4928.
(9) Lee, J. W.; Hall, A. S.; Kim, J.-D.; Mallouk, T. E. *Chem. Mater.* **2012**, *24*, 1158−1164.
(10) Zhang, Y. C.; Qiao, T.; Hu, X. Y. *J. Solid State Chem.* **2004**, *177*, 4093−4097.
(11) Ahmed, K. A. M.; Peng, H.; Wu, K.; Huang, K. *Chem. Eng. J.* **2011**, *172*, 531−539.
(12) Wu, Y.-T.; Hu, C.-C. *Electrochem. Solid State Lett.* **2005**, *8*, A240−A244.
(13) Chang, Y. Q.; Yu, D. P.; Long, Y.; Xu, J.; Luo, X. H.; Ye, R. C. *J. Cryst. Growth* **2005**, *279*, 88−92.
(14) Zhang, Y.; Wang, N.; Gao, S.; He, R.; Miao, S.; Liu, J.; Zhu, J.; Zhang, X. *Chem. Mater.* **2002**, *14*, 3564−3568.
(15) Comini, E. *Anal. Chim. Acta* **2006**, *568*, 28−40.
(16) Zhang, B.; Jung, Y.; Chung, H. S.; Vugt, L. V.; Agarwal, R. *Nano Lett.* **2010**, *10*, 149−155.
(17) Moon, G. D.; Ko, S.; Min, Y.; Zeng, J.; Xia, Y.; Jeong, U. *Nano Today* **2011**, *6*, 186−203.
(18) Park, W. I.; Kim, H. S.; Jang, S. Y.; Park, J.; Bae, S. Y.; Jung, M.; Lee, H.; Kim, J. *J. Mater. Chem.* **2008**, *18*, 875−880.
(19) Long, H.; Fang, G. J.; Huang, H. H.; Mo, X. M.; Xia, W.; Dong, B. Z.; Meng, X. Q.; Zhao, X. Z. *Appl. Phys. Lett.* **2009**, *95*, 013509.
(20) Paracchino, A.; Laporte, V.; Sivula, K.; Grätzel, M.; Thimsen, E. *Nat. Mater.* **2011**, *10*, 456−461.
(21) Cheng, W.-Y.; Lin, Y.-F.; Lu, S.-Y. *Appl. Phys. Lett.* **2011**, *99*, 063107.
(22) Willinger, M.-G.; Neri, G.; Rauwel, E.; Bonavita, A.; Micali, G.; Pinna, N. *Nano Lett.* **2008**, *8*, 4201−4024.
(23) Marichy, C.; Donato, N.; Willinger, M.-G.; Latino, M.; Karpinsky, D.; Yu, S.-H.; Neri, G.; Pinna, N. *Adv. Funct. Mater.* **2011**, *21*, 658−666.
(24) Na, C. W.; Woo, H.-S.; Kim, I.-D.; Lee, J.-H. *Chem. Commun.* **2011**, *47*, 5148−5150.
(25) Na, C. W.; Woo, H.-S.; Lee, J.-H. *RSC Adv.* **2012**, *2*, 414−417.
(26) Hwang, I.-S.; Choi, J.-K.; Kim, S.-J.; Dong, K.-Y.; Kwon, J.-H.; Ju, B.-K.; Lee, J.-H. *Sens. Actuators, B* **2009**, *142*, 105−110.
(27) Na, C. W.; Woo, H.-S.; Kim, H.-J.; Jeong, U.; Chung, J.-H.; Lee, J.-H. *CrystEngComm* **2012**, *14*, 3737−3741.
(28) Wang, Z. L. *J. Phys.: Condens. Matter* **2004**, *16*, R829.
(29) Malavasi, L.; Galinetto, P.; Mozzati, M. C.; Azzoni, C. B.; Flor, G. *Phys. Chem. Chem. Phys.* **2002**, *4*, 3876−3880.
(30) Thimsen, E.; Peng, Q.; Martinson, A. B. F.; Pellin, M. J.; Elam, J. W. *Chem. Mater.* **2011**, *23*, 4411−4413.
(31) Schumm, M.; Koerdel, M.; Müller, S.; Ronning, C.; Dynowska, E.; Gołacki, Z.; Szuszkiewicz, W.; Geurts, J. *J. Appl. Phys.* **2009**, *105*, 083525.
(32) Woo, H.-S.; Na, C. W.; Kim, I.-D.; Lee, J.-H. *Nanotechnology* **2012**, *23*, 2445501.
(33) Liu, Y.; Koep, E.; Liu, M. *Chem. Mater.* **2005**, *17*, 3997−4000.
(34) Morrison, S. R. Chemical sensors. In *Semiconductor Sensors*; Sze, S. M., Ed.; John Wiley & Sons, Inc.: New York, 1994; pp 383−413.
(35) Ghosh, M.; Raychaudhuri, A. K. *Nanotechnology* **2008**, *19*, 445704.
(36) Fan, Z.; Wang, D.; Chang, P. C.; Tseng, W. Y.; Lu, J. G. *Appl. Phys. Lett.* **2004**, *85*, 5923−5925.
(37) Barsan, N.; Simion, C.; Heine, T.; Pokhrel, S.; Weimar, U. *J. Electroceram.* **2010**, *25*, 11−19.
(38) Cho, N. G.; Woo, H.-S.; Lee, J.-H.; Kim, I.-D. *Chem. Commun.* **2011**, *47*, 11300−11302.
(39) Pillai, U. R.; Deevi, S. *Appl. Catal. B: Environ.* **2006**, *64*, 146−151.
(40) Borck, Ø.; Hyldegaard, P.; Schroder, E. *Phys. Rev. B* **2007**, *75*, 035403.
(41) Xie, X.; Li, Y.; Liu, Z.-Q.; Haruta, M.; Shen, W. *Nature* **2009**, *458*, 746−749.